Journal of Power Sources 555 (2023) 232383

Contents lists available at ScienceDirect

Journal of Power Sources

journal homepage: www.elsevier.com/locate/jpowsour

Water cluster characteristics of fuel cell gas diffusion layers with artificial microporous layer crack dilation

Daniel Niblett [a,*], Vahid Niasar [b], Stuart Holmes [b], Adrian Mularczyk [d], Jens Eller [d], Robert Prosser [c], Mohamed Mamlouk [a]

[a] School of Engineering, Newcastle University, NE1 7RU, United Kingdom
[b] Department of Chemical Engineering, University of Manchester, Manchester, M13 9LP, United Kingdom
[c] Department of Mechanical, Aerospace and Civil Engineering, University of Manchester, Manchester, M13 9LP, United Kingdom
[d] Paul Scherrer Institut. Forschungsstrasse 111, 5232 Villigen, PSI, Switzerland

GRAPHICAL ABSTRACT

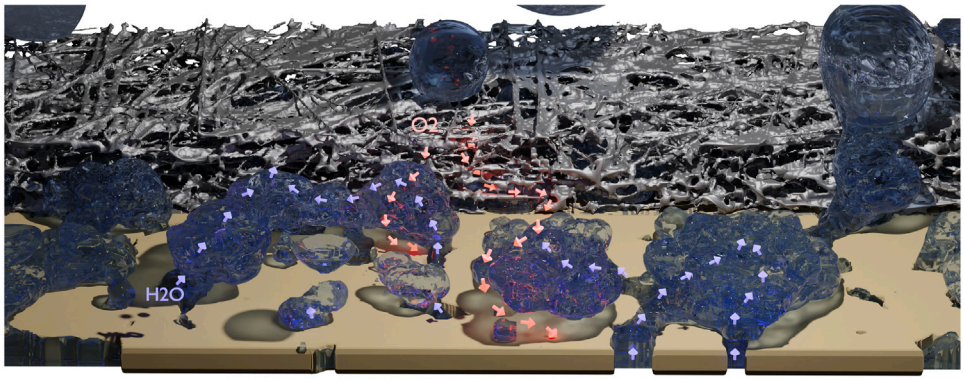

HIGHLIGHTS

- Volume of fluid simulation is validated against X-ray CT data with 88% match.
- Water clusters inside the GDL can merge in-plane before emerging to the channel.
- 3D contact angles extracted from CT images show heterogeneous wettability.
- Microporous layer cracks can impact water flooding in the gas diffusion layer.
- Oxygen transport to the catalyst layer is impacted by water distribution.

ARTICLE INFO

Keywords:
Gas diffusion layer
Water clusters
Volume of fluid
MPL cracks
Water management

ABSTRACT

The formation of discrete water clusters in polymer electrolyte fuel cell gas diffusion layers (GDL) can lead to increased resistance for oxygen transport in the catalyst layer. This study investigates the effect of MPL crack propagation on the water cluster development in a X-ray computed tomography (CT) microstructure using the volume-of-fluid method (VoF). The VoF calculation was compared to operando CT data by voxel matching, obtaining a maximum 88 % accuracy. Using 3D contact angle extraction, the local scale heterogeneous wettability in the GDL was investigated. In a simulation study, MPL cracks were created as the boundary sources for water and the effect of increasing the area fraction covered by cracks on the water distribution

* Corresponding author.
E-mail address: daniel.niblett@newcastle.ac.uk (D. Niblett).

https://doi.org/10.1016/j.jpowsour.2022.232383
Received 5 August 2022; Received in revised form 2 November 2022; Accepted 7 November 2022
Available online 19 November 2022

in the GDL was investigated. The increased cracking, created larger discrete water clusters in the GDL with greater connectivity, due to in-plane coalescence. The in-plane movement leads to coalescence of clusters, forming fewer, larger clusters at later times close to breakthrough to the channel. This phenomena is shown by the decrease in water cluster density (n mm^{-2}) from 10 to 5. This immobile water impacts the distribution of oxygen at the catalyst layer (10 % local difference) and therefore the current density distribution.

1. Introduction

In polymer electrolyte fuel cells (PEFC) several material layers are required to distribute reactants (hydrogen and oxygen) and products (water, heat and electricity) of the electrochemical reaction. During certain operating conditions (such as during high current density operation), the structure of these layers can impact the performance of the cell as a result of water flooding (as shown by the concentration gradient in Fig. 1(a)). Understanding the development of discrete water clusters in this system which form as a consequence of the surrounding materials is important for design and operation of fuel cells [1]. Therefore, the coupling between the gas diffusion layer (GDL), gas channel (GC) and microporous layer (MPL) is important because the interfaces can facilitate or hinder mass transport of oxygen to reach the catalyst layer [2,3].

Water accumulation in the GDL in the form of discrete water clusters decrease the effective diffusivity of the system since the tortuosity of the air phase is increased by their presence [4]. This effect is illustrated by the oxygen concentration distribution around the white water clusters shown in Fig. 1(a). They also contribute to further flooding in the CL, due to blocking the area for diffusion by through the pathways at the MPL/GDL interface. Furthermore, the air flow distribution in the flow fields and GDL could be impacted by the presence of water, possibly leading to heterogeneity in air velocity distribution which feeds the entire cell, potentially leading to regions of diffusion limited transport of oxygen [5].

Water clusters in the GDL provide the pathways of water flow to the gas channel flow fields [1,6–10]. They also control water removal from catalyst layer which can cause oxygen starvation, flooding, non-uniform current distribution and degradation. Oxygen starved regions will undergo degradation due to differences in reaction rates and temperature gradients and consequently it is important to resolve water cluster topology in different GDL microstructures [11] which contribute to these scenarios.

As highlighted by Fig. 1(b), water may appear from MPL cracks due to its hydrophobic wettability. They form preferential pathways for water to enter the GDL from the MPL/CL and therefore water clusters can be disconnected with independent water phase pressures [12]. Water then percolates through the fibrous porous network to the flow field channels (or rib regions) as shown by Fig. 1(b) where both microstructure and wettability effect water accumulation. Depending on the spatial distribution of these MPL cracks and the wettability of the channels, the water may attach and spread on the rib surfaces. Cracks in the MPL surface as shown by Fig. 1(c) may change in size due to degradation processes [13], which will increase the available area for water injection, and potentially lead to more independent water clusters emerging into the GDL.

However, it is difficult to study the interaction of these materials with water since these processes occur micro-scales inside opaque materials. Due to the difficulty in experimental imaging, set up and controlled MPL cracking, it is difficult to use ex-situ methods to perform sensitivity analysis on the materials. Furthermore, the appearance of water, as either a boundary source or a condensation source is difficult to quantify and control. In ex-situ experiments the inlet condition of water is from either discrete sources (e.g. hydrophobic MPL cracks or condensation [14]) as shown in Fig. 1(c) or applied as a full area injection (e.g. Water reservoir experiments [15]).

Liquid water transport is further complicated by the region of interest either under the rib or channel (e.g. at high humidity, under the rib regions, water appears from condensation nucleation points [16,17]). X-ray CT experiments show discrete water clusters forming both under the channel and rib regions [12,14,18–21]. Under different boundary conditions porous GDL microstructures can create different water cluster topology [14,22,23]. Therefore, evaluating process characteristics (such as saturation and effective diffusivity) in conditions closely resembling operating fuel cell conditions is essential to increase the applicability of the results to aid in fuel cell design. This is especially important to reduce cell cost and lifetime by opening the operating window to high current density 2 A cm^{-2}, where water distribution in the porous layers effect the distribution of oxygen [24]. This can be achieved by simulation of water transport in current and future materials which can develop strategies for the design of novel materials for water management [5,25].

Experimental studies show material degradation can affect the performance of fuel cells [26,27]. During cycling, catalyst and MPL cracks can propagate and expand, creating a fractured surface. MPL crack dilation has been shown to be possible during the lifetime operation of PEFC at different locations across the cell [13]. An example of this possible degredation induced crack dilation is shown in Fig. 1(c). The MPL cracks have a much larger pore dimension (μm) than the surrounding MPL pores (nm) and have shown to provide pathways for water transport to the GDL [28]. However, the impact of increased MPL cracking on water accumulation in GDL has not been investigated. The area coverage of the cracks on the MPL are shown to be normally between 2%–8% [29]. However, the effect of extreme cracking scenarios (between 14%–100% MPL area covered by cracks (i.e. no MPL)) caused by long term degradation [13] has not been studied so far. This would be challenging experimentally to perform due to the difficulty of controlled cracking of MPL, as well as the technical complexity of X-ray imaging [14,18,19].

The presence of MPL cracks is generally accepted to improve water management [28–34]. However, the impact of crack area fraction on water accumulation in the GDL has not been studied. Each discrete water cluster emerging from these MPL cracks has its own phase pressure [18,22,35] and the water cluster density, defined as the number of water clusters per in-plane area of material is important for flooding in the channels and water covering the GDL for oxygen transport [1]. This interaction of the GDL-channel interface cannot be ignored, as the water covering the GDL surface blocks oxygen transport [1,36,37].

Therefore one approach is to use computational fluid dynamics (CFD) to resolve the porous microstructure from CT images and simulate water interaction knowing the surface wettability. The volume-of-fluid method (VoF) is an interface resolving technique to simulate water–air two-phase flow with interaction with solid surfaces using the finite volume method [38]. It was used in previous studies [23] to compare the spatial water topology in SGL 25 BA with CT data with a 92% spatial distribution of water match. It was further used to compare dynamic capillary pressure profiles from water simulation in Toray TGP-H 060 to an image analysis prediction of capillary pressure from the CT data [12] with good agreement.

There are a number of methods that can simulate and study two-phase flow in fuel cell GDL ranging from pore-network models [3,16,39–43], lattice-Boltzmann models [8,32,44,45] to VoF [15,23,46]. There are general advantages and disadvantages of each method for example pore network models are extremely computationally efficient due to the extraction of a pore space into network of linear connections. However, they simplify the geometric space and it is challenging to account for sub-pore scale variation in microstructure and wettability

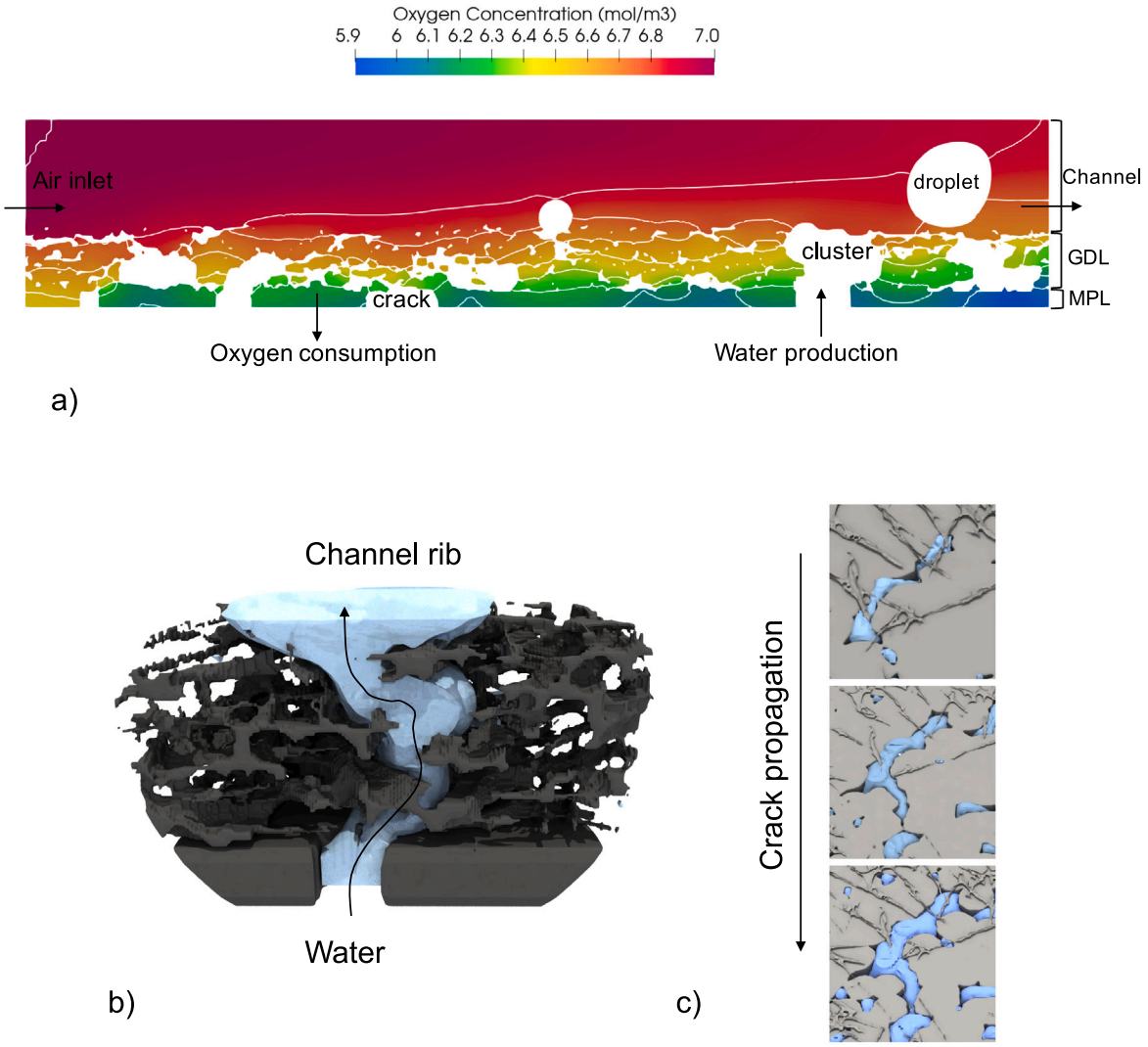

Fig. 1. (a) Visualisation of oxygen transport and consumption with the effect of water distribution in the gas diffusion layer (Toray) and channel. Oxygen consumption is at the microporous layer (MPL) boundary with water appearing from MPL cracks. (b) Rendering of water cluster percolation from a MPL crack through the Toray GDL and attachment to channel-rib region. (c) propagation of an artificial MPL crack used in the simulations between 2%–14% area coverage.

that could effect the flow [47]. Lattice-Boltzmann models are explicit methods and have the advantage that they can use the voxel grid directly without computational meshing however, there are difficulties that limit the general application of LBM to different scenarios as explained in Ref. [48]. The VoF utilising finite volume method can be applied to small and large scale systems efficiently with a multi-resolution mesh conforming to solid surface structures. It has been validated in a variety of flow and interfacial flow phenomena outside the area of electrochemical devices [49] and for water droplet dynamics in fuel cell channels and GDL [23,36]. However, due to the small time step limited by the advection of the volume fraction through the computational cells, the simulations can be computationally expensive, requiring between 1–5 weeks on 32 processors [23].

In terms of validation of computational models, only a handful of studies have compared the exact spatial distribution of water against experimental results [23,40,45,50]. Further analyses of this kind is beneficial to test the validity of computational models and the comparison between experimental and simulation results is useful for several reasons:

1. to demonstrate predictive capabilities of models beyond experimental validation so that new designs and structures can be created.
2. to achieve a robust modelling approach to complement time and cost demanding experiments.
3. to assess validity of commonly used assumptions in modelling studies and improve modelling workflows.
4. to link the localized oxygen distribution to the current/voltage distribution in CL. This allows the study of the effect of MPL mechanical degradation on CL degradation caused by oxygen starvation.

While in earlier studies by the authors [12] only a limited extent of the available CT data was used (as shown by the yellow volume in Fig. 2(a)), herein the full CT data sets are used for CFD simulations. The purpose of this study is to investigate the development of discrete water clusters in response to material degradation in the form the microporous layer crack network expansion, with the presence of the gas channel. X-ray computed tomography microstructure and transient water volume data are provided from authors previous studies [12]. Details regarding the estimated local surface wettability are extracted using this data.

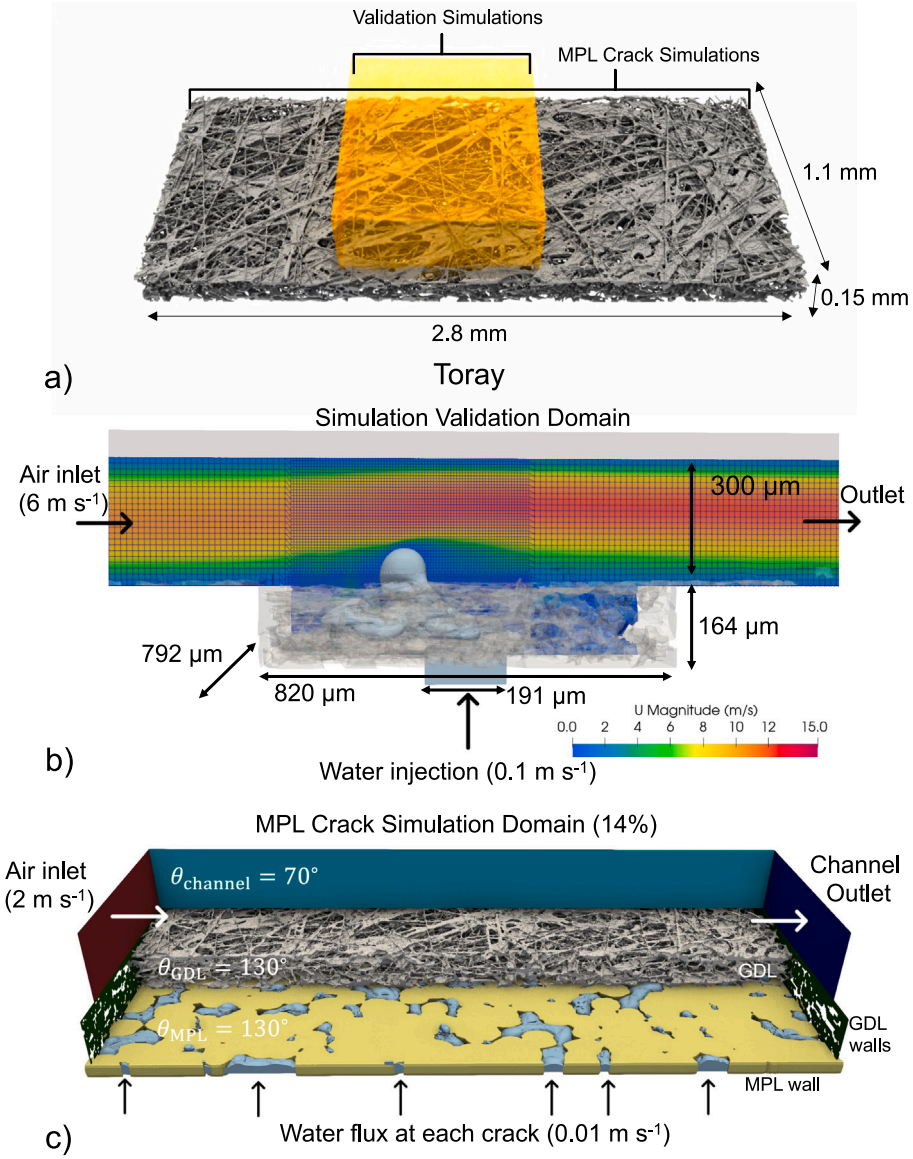

Fig. 2. (a) Dimensions of CT rendered surfaces for Toray TGP H-060 with the areas for the validation (yellow) and MPL crack simulations highlighted. Simulation domain and boundary conditions for (b) the simulation validation against CT data and (c) the full CT image with generated MPL crack simulations. A subset of the CT image was used for the validation simulation to increase computational efficiency. (For interpretation of the references to colour in this figure legend, the reader is referred to the web version of this article.)

2. Methodology

2.1. Materials

X-ray Computed tomography images of Toray TGP-H 060 and operando water distribution was obtained from authors previous study, where the detailed experimental imaging set up can be found [12]. However, it is important to iterate the measurement conditions to highlight possible differences between the predictive model and experimental results. The GDL had a coating of 10 wt % coating of polytetrafluoroethylene (PTFE) without an MPL and was placed on top of a catalyst coated membrane (CCM). This was a Gore Primea membrane (15 µm thickness) with 0.1 and 0.4 mg cm^2 loading on the anode and cathode respectively. The emergence location of water clusters was controlled by laser ablation of the CCM to an area of 200 × 250 µm active area. The cell was operated under fully humidified conditions at 32 °C with a flow rate of 6 m s^{-1} oxygen in the flow channel.

This study extracted the solid surface from segmented X-ray CT images of Toray TGP-H 060 [12] (2.8 ×1.1× 0.15 mm^3 at 2.75 µm voxel size) to generate a surface triangulated file as shown in Fig. 2(a). The yellow volume shown in Fig. 2(a) was taken as a subset of the full CT image to create the simulation domain in Fig. 2(b). The full CT image was then used for MPL cracking scenario simulations as shown in 2(c).

The Toray material did not have a MPL but the CL in the experiment will have a pore network unresolved by the X-ray CT. For the validation simulations, a block was used below the extracted GDL microstructure, with an open area equivalent to the size of the active area. For the MPL cracking simulations, the open areas were transformed into cracks with sizes resembling those found in literature [29].

The water injection was not connected underneath the MPL and so did not have a connected phase pressure. The method for generating the artificial cracks is as follows: the last image of the segmented CT dataset was extracted (1001 × 400 × 1 voxels) and circles of 4 voxels in radius were mapped onto the voxel grid by comparing the euclidean distances of circle and voxel coordinates. As shown by Fig. 3(a) 500 solid overlapping circles were distributed on the surface. Next the

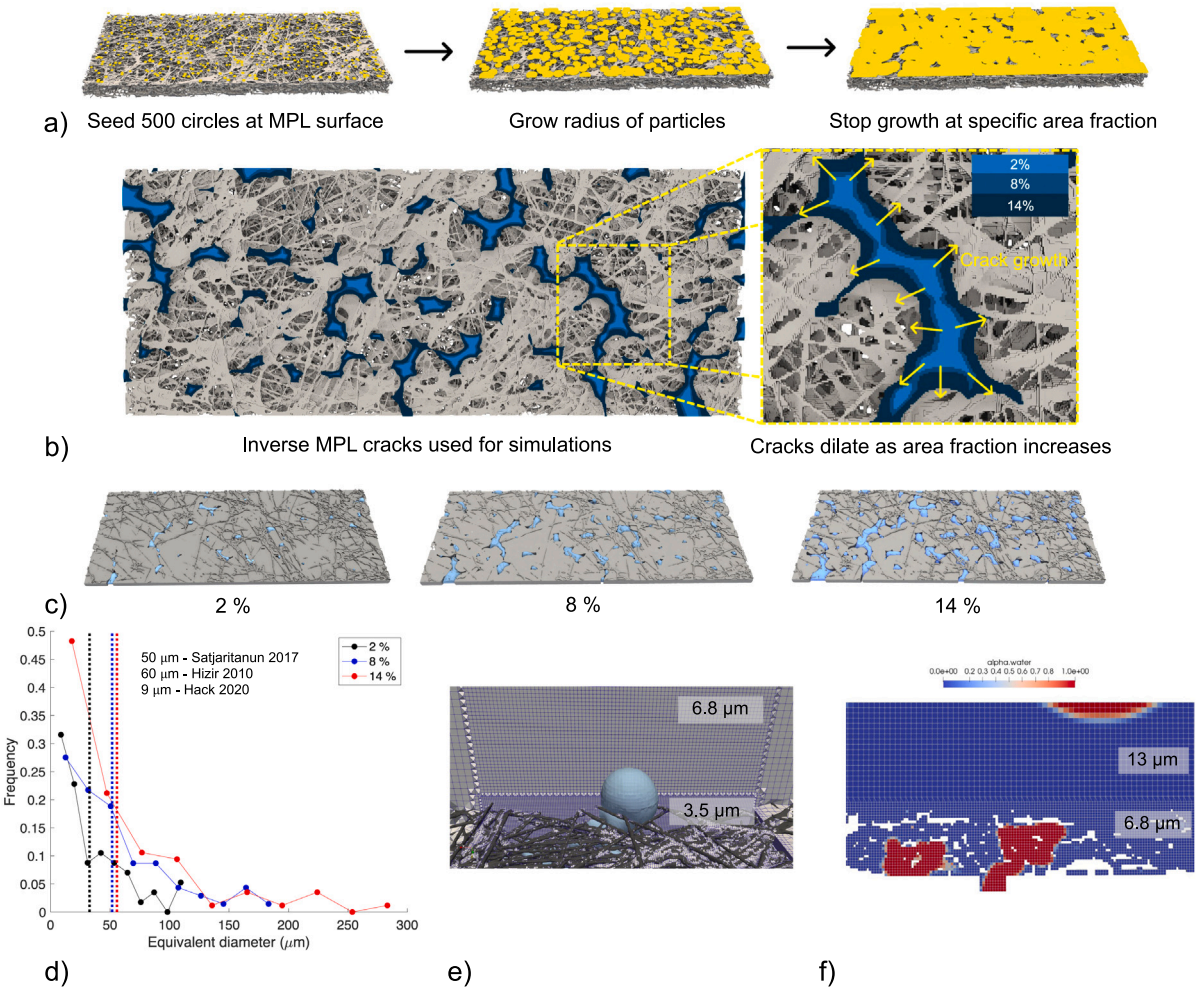

Fig. 3. (a) process generating MPL cracks with different area fractions by seeding particles on the last CT image and growing particle radius. (b) GDL microstructure with crack positions and specific crack growth shown from light to dark blue. (c) Final MPL crack boundary conditions for water injection into the GDL. (d) MPL crack size distribution (equivalent circular radius) for each MPL crack scenario tested (2, 8 and 14%), with dashed lines showing average crack size. (e) Computational mesh used for the comparison between VoF and CT data. (e) computational mesh used for MPL cracking scenarios with cell resolution highlighted. (For interpretation of the references to colour in this figure legend, the reader is referred to the web version of this article.)

radius of particles was increased, until specific MPL area fractions was established. Three different MPL crack area coverage fraction were used as injection boundary conditions as shown in Fig. 3(c) ranging from 2, 8 and 14% in terms of area coverage. This approximates the dilation of MPL cracks without the need of a physical model as shown in Fig. 3(b). Three different MPL crack area coverage fraction were used as injection boundary conditions as shown in Fig. 3(c) ranging from 2, 8 and 14% in terms of area coverage. Analysis of the cracks was imported into a custom code using a MATLAB based porous microstructure generator [51], to extract the MPL crack distribution which had a similar crack size to that reported in literature [13,29,32].

2.2. Contact angle extraction

The intrinsic contact angle which would be most appropriate for use in computational simulation was not used because it was not available at the time of simulation. The sessile drop method was used to obtain an approximation of the internal contact angles which was used as the boundary condition for the VoF simulation. However to understand the real intrinsic wettability of the microstructure, 120 time steps of CT images were processed to extract the distribution of contact angles. The voxels of the solid and water interface were smoothed to a surface. The normals of each vertex were calculated and vertices (between solid and water interface) were linked based on a distance of 1 voxel. This ensured that the triple line was not used. This is important as during the smoothing procedure of voxels, surfaces become parallel (180°) at the triple point. The angle between the normal vectors was calculated as the contact angle. The code was tested against an artificial droplet with varying contact angles, calculated using the radius of curvature change [1]:

$$R = \left(\frac{3V}{4\pi(2+\cos(\pi-\theta))(1-\cos(\pi-\theta))^2} \right)^{1/3} \quad (1)$$

where θ is the liquid contact angle on the solid surface, and V is the volume of the droplet. This droplet was mapped onto a voxel grid and the contact angles were extracted. This produced an error of 10° as shown in Fig. 5(a). This algorithm is similar to that used in [45] to extract the internal contact angles of the GDL but instead uses the CT image directly.

The algorithm was used on each time step of CT data of water moving through the porous microstructure, requiring around 30 s per image. The average distribution and fraction of the surface which corresponds to a particular contact angle is shown in Fig. 5.

2.3. Numerical method

This study used computational fluid dynamics (CFD) and the volume of fluid method (VoF) to solve two-phase flow of liquid water and air

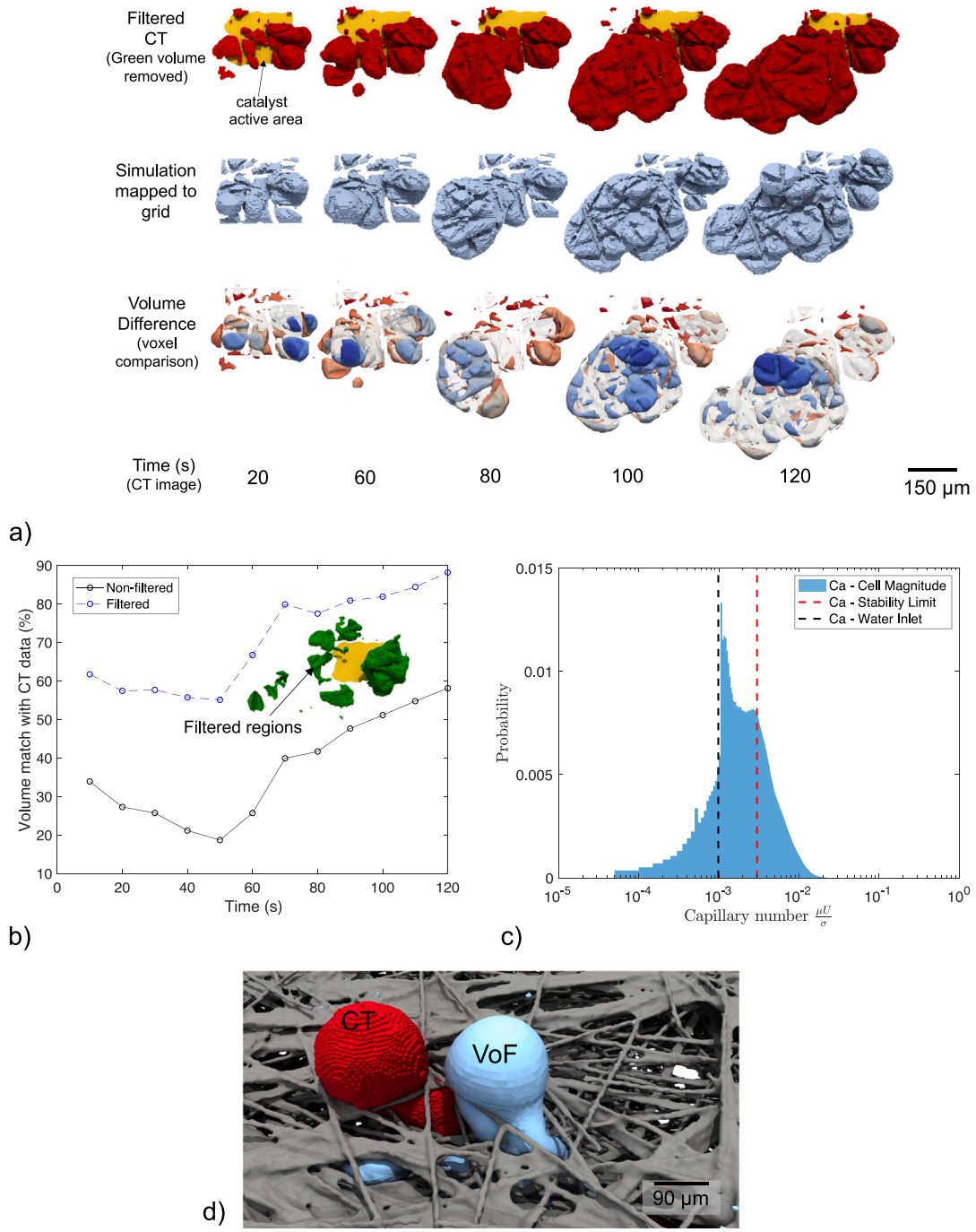

Fig. 4. (a) 3D water volume renderings showing the comparison between simulation mapped to CT grid (blue) and CT water data (red) with filtered regions removed (Fig. 4(b)). This includes the voxel comparison result with height extent shown as colour gradient and with scale bars shown. (b) Simulation volume match with CT data with non-filtered and filtered data. Green volume shows the filtered regions where the simulation could not enter those flow paths. (c) Capillary number distribution for all water cells and all time steps. (d) Comparison of the channel emergence location of both CT and simulation with scale bar shown. (For interpretation of the references to colour in this figure legend, the reader is referred to the web version of this article.)

in a transient simulation. Additionally, oxygen transport (convection–diffusion–reaction) is simulated in a steady-state snap-shot of water in the complex porous system. The VoF method is a robust interface tracking method, able to simulate free-surface flows such as water and droplet or bubble flows in liquids with different density or viscosity on computational grids that can resolve surface structures [38,52]. It involves the transport of a volume fraction scalar through a computational grid using an advection equation, where a value of 1 represents water, and 0 represents air. At the water–air interface, alpha in the cells is a fraction of both, which indicates the interfaces lies within the cell. Properties used in solving the Navier–Stokes equations (density and viscosity) are updated at every time step to account for this. Accurate advection of the volume fraction requires amendment of the transport equation and knowledge of the cell interface normal and curvature through either geometric (isoAdvector) or algebraic methods which have different advantages which are more clearly discussed in [38].

To simplify the computation, phase change and gravitational acceleration were not included and furthermore, multi-species diffusion and pressure drop due to oxygen consumption was not considered due to

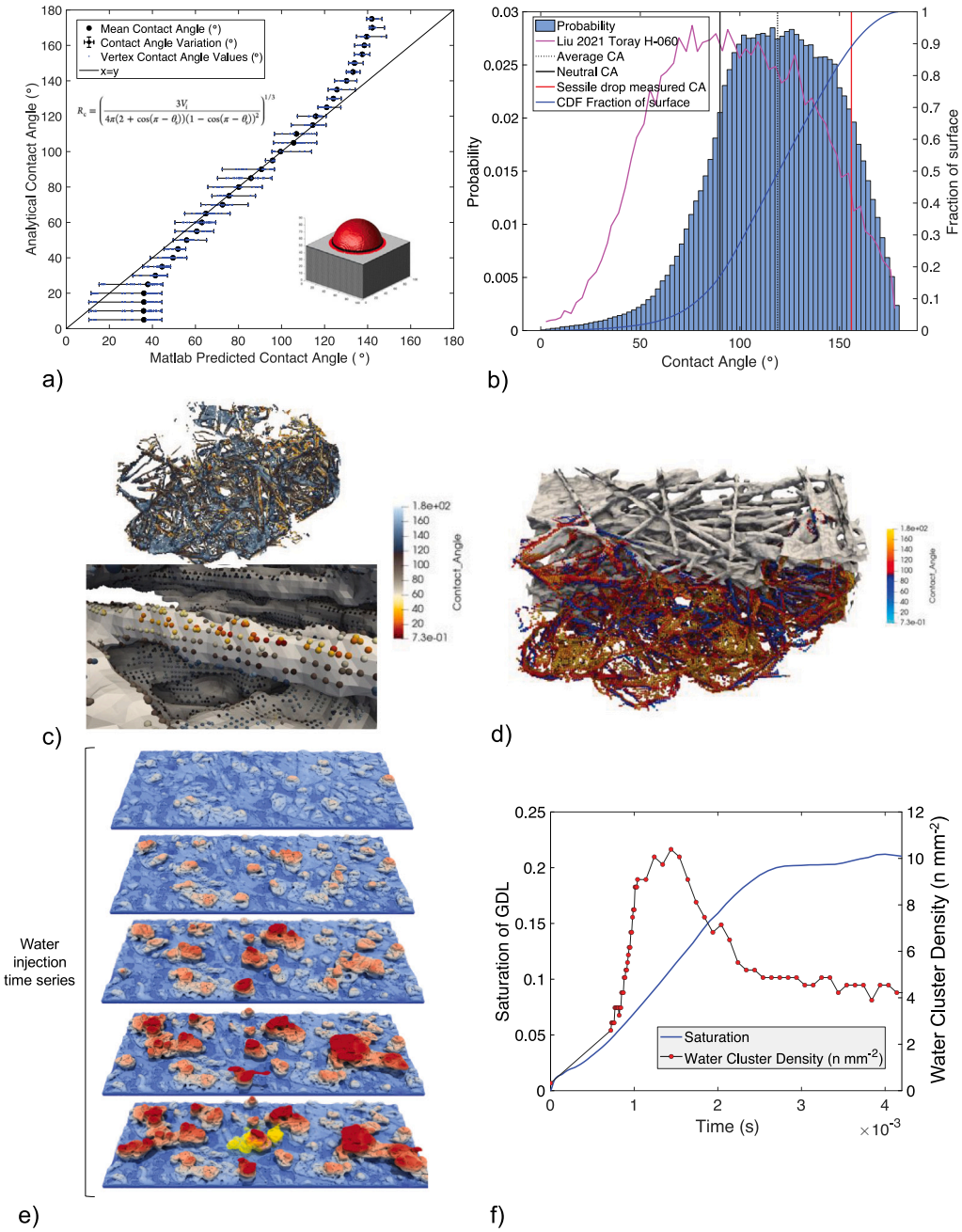

Fig. 5. (a) sensitivity analysis of the developed 3D contact angle extraction code. (b) histogram of probability and cumulative (blue line—fraction of surface) contact angle distributions for all surfaces the structure where there is an interface. Results are averaged over 120 time steps, with other lines representing neutral contact angle (dashed at 90°), mean contact angle (dotted at 118°) and measured contact angle (red at 156°). Data for a similar Toray material reported by Liu 2021 et al. [45] shown in magenta. (c) and (d) 3D rendering of the internal surface of the GDL microstructure with extracted contact angles saved as spheres with a coloured contact angle. (e) Water injection time series for 100% area injection into Toray GDL and (f) showing GDL saturation and water cluster density (n mm^{-1}). (For interpretation of the references to colour in this figure legend, the reader is referred to the web version of this article.)

the small domain size. The flow is assumed to be isothermal, incompressible, laminar flow. The governing equation for mass conservation solved in each cell is:

$$\nabla \cdot \mathbf{u} = 0 \tag{2}$$

where $\mathbf{u}$ is the velocity vector. The momentum equation for fluid flow, excluding gravity but including interface forces is represented by the Navier–Stokes equations as:

$$\rho \frac{\partial \mathbf{u}}{\partial t} + \rho \nabla \cdot (\mathbf{u}\mathbf{u}) = -\nabla p + \nabla \cdot (\mu(\nabla \mathbf{u} + \nabla \mathbf{u}^T)) + F_\sigma \tag{3}$$

where p is the pressure, ρ is the density and μ is the viscosity. These physical properties are determined by the volume fraction of water in each cell α, for example the average cell viscosity is: $\mu = \alpha\mu_1 + (1-\alpha)\mu_2$. The volumetric interfacial force F_σ is calculated as:

$$F_\sigma = \sigma\kappa(\alpha)\nabla\alpha \tag{4}$$

where the interface curvature in each cell is estimated using the vector of the cell face $\mathbf{S_f}$ and the unit normal vector:

$$\kappa = -\nabla \cdot \left(\frac{\nabla\alpha}{|\nabla\alpha|} \cdot \mathbf{S_f} \right). \tag{5}$$

The scalar volume fraction is transported using the general transport equation for advection.

$$\frac{\partial \alpha}{\partial t} + \nabla \cdot (\alpha \mathbf{u}) = 0 \tag{6}$$

Different interface capturing or advection schemes can be used for the advection of α in order to obtain a sharp interface. In this study, OpenFOAM was used along with the isoAdvector volume of fluid method [52,53]. Details of this method and its features have been thoroughly documented in Ref. [23,52]. However, it is important to highlight some of the challenges and features of the volume of fluid method. The VoF method is a mass conservative method although, spurious currents can be generated around the interface, causing numerical diffusion of the volume fraction [49]. Geometrical interface advection schemes with piece-wise linear interface reconstruction (PLIC) [38] or filtering of interface velocity can reduce these values significantly compared to the standard interFoam solver in OpenFOAM [49].

The formulation used for the contact angle boundary condition at the contact line uses the specified contact angle θ and normal vectors of the interface $\mathbf{n}$ and walls $\mathbf{n_s}$:

$$\mathbf{n} \cdot \mathbf{n_s} = \cos(\theta) \tag{7}$$

This method is a simplification for equilibrium conditions and does not account for advancing and receding contact angles under highly dynamic states. However, because the water flow is slow, dynamic states would only be found during droplet detachment in the channel and therefore was not considered. The simulations were completed with the same computational settings as authors previous studies (CFL 0.1, snapTol 0, nAlphaBounds 3, clip false, tolerance for velocity, pressure, alpha 10^{-9}) [23].

To investigate the effect of water and microstructure on the oxygen distribution, steady-state transport of a passive scalar was solved using a steady-state velocity field found using the simpleFoam solver, similar procedure to that performed in Ref. [5]:

$$\nabla \cdot (\mathbf{u}C) - \nabla \cdot (\mathrm{D}\nabla C) = 0 \tag{8}$$

The oxygen concentration C (7.1 mol m^{-3}) is transported through the air space domain by a combination of molecular diffusion, with the diffusion coefficient D (2×10^{-5} m^2 s^{-1}) and convection from the velocity field u. In these cases, the water phase was converted into a solid boundary to approximate a snapshot in time (therefore it was not necessary to stop the diffusion of oxygen into water). At the MPL boundary, a fixed gradient condition is applied to approximate the passive scalar consumption at a current density i of 1 A cm^{-2}:

$$\nabla C = -\frac{i}{4F\mathrm{D}_{\mathrm{MPL}}} \tag{9}$$

where F is the Faraday constant and $\mathrm{D}_{\mathrm{MPL}}$ is the effective diffusion coefficient in the MPL (assumed to be 5.05×10^{-5} m^2 s^{-1}) and the number of electrons exchanged in the oxygen reduction reaction at the cathode catalyst layer is 4. The convergence criteria for the steady state flow and transport simulations was set to be 1×10^{-5}. The external walls and GDL surfaces had no slip velocity and zero gradient in pressure and concentration boundary conditions applied. At the outlet, a pressure value of 0 Pa, zero gradient velocity and concentration was applied. The velocity field used for oxygen advection was at steady-state, assuming the water was static, which was assumed to be valid because the water flux (1×10^{-5} m s^{-1}) is much lower than the air flux (1 m s^{-1}) under real operating conditions. This was performed to reduce the complexity of the computational model.

2.4. Domain generation

The simulation domain consists of the gas channel and gas diffusion layer with discrete injection locations provided by the microporous layer cracks as shown by Fig. 2(b). The 3D CT voxel structure was smoothed and meshed using snappyHexMesh to generate the computational domain. For the comparison between VoF and CT data, the water inlet was assumed to be equal to the area of the dimensions of catalyst active area as shown by the yellow patch in Fig. 4(a).

The mesh was refined in three different areas for computational efficiency (coarse: external channel 13 μm, medium: channel region at droplet emergence 6.8 μm, fine: porous region for water 3.5 μm) as shown in Fig. 3(e) and (f). The GDL contact angle was 156° [12] which was applied homogeneously on the solid surfaces. The inlet velocity of water (from the catalyst active area) and air (from the inlet of the channel) was 0.1 and 6 m s^{-1} respectively. The simulation required approximately 5 weeks on 28 CPU (Intel Xeon E5-2640 0 @2.50 GHz) with approximately 2 million grid cells to reach breakthrough to the channel. This was because the adaptive time step was low and the time required for water percolation to reach the channel was long, meaning many iterations for the transient simulations were needed.

The simulation and CT image were compared at timesteps when the volume of water in the GDL was equal. However, due to mechanisms not included in the simulation (unresolved mesh regions, phase change or connected water pathways in the catalyst layer), the green region in Fig. 4(c) appeared early. Therefore, to provide a much closer comparison as shown by the images in Fig. 4(b), this was filtered out to remove the time lag in the simulation data to focus in the analysis on the main water percolation pathways in the CT data.

The computational grid for the MPL cracking scenarios used a coarse to medium mesh refinement as shown in Fig. 3(f). This was chosen to increase computational speed because the simulation domains were larger. The domain contained 1.96 million cells, with the smallest cell resolution of 6 μm (with results shown in Figs. 5(e) and 6).

The pore structure developed from this coarser mesh may not replicate local scale fluid dynamics such as the laminar boundary layer between tight pore throats. However, we are focused on capillary dominated two-phase flow and this mesh preserves the general porous structure of the larger network of pores. Small pores would not receive much change in flow rate, because of the hydrophobic surfaces. To decrease simulation time, a water injection rate of 0.01 m s^{-1} (536 A cm^{-2}) was applied to the water inlet surface at the microporous layer. This is possible because the development of the water flow paths is independent of the water velocity below a capillary number threshold [23,32].

2.5. Assumptions

The model assumes unsteady, laminar, isothermal and incompressible flow which is valid considering the scale and Reynolds numbers experienced (Re < 1). The internal surfaces of the Toray material was set as the measured contact angle (156°) and the contact angle for the porous microstructure for the MPL crack simulations (shown in Fig. 6) was assumed to have a lower homogeneous contact angle of 130° which was set due to the differences in the measured contact angle and the distribution extracted in Fig. 5. The loss of the GDL contact angle over cell lifetime is a known issue [54] resulting in performance loss from water accumulation induced degradation.

Previous studies have shown the volume of fluid method cannot practically replicate the exact dynamic time series data until breakthrough to the gas channel because the time step required for stable simulation is very low ($t = 10^7 - 10^9$ s) [23]. However, as shown by the results in this study, the VoF method provides an accurate way to predict the microstructure water distribution relationship. Therefore, to study the interaction between the solid structure and water over 120 s of real time, the simulation was accelerated (by increasing the water flux). The capillary number exhibited by this increased flow rate was chosen to ensure the flow remains capillary dominated (so that the flow paths are not influenced by fluid convection). However, this capillary number was chosen for the inlet area whereas the local capillary number could be much larger due to pore scale constrictions.

The increase in the flow rate may lead to an increase in inlet pressure which could affect how water moves through the porous network. However, as shown in authors previous study for the same data set, the phase pressure of water in the simulation was very similar to the extracted phase pressure calculated purely using curvature analysis and Young–Laplace equation [12].

2.6. Post-processing

Comparison of water volume data between simulation and CT was only performed until breakthrough to the gas channel as shown in Fig. 4. The simulation did not resolve some flow paths in the porous network which could be related to real connected pathways in the CL not resolved in the computational mesh [12]. Therefore, to understand the potential of VoF for replicating the water cluster a comparison was made between the CT data and the simulation data with the unrepresented pathways and with them removed (filtered data).

To compute the comparison between the spatial distribution of the water for both simulation and experiment, the simulation data (volume fraction) was mapped to a voxel grid with the same dimensions as the CT image shown in Fig. 4(a). The same process was also used to create the averaged water thickness maps and the water subtraction processes are depicted in Fig. 6(a).

To assess our choice of accelerating the water injection rate, the capillary number distribution for each cell in the validation simulation domain which contained water was extracted using:

$$\mathrm{Ca} = \frac{\mu U_i}{\sigma} \tag{10}$$

Where μ is the viscosity of water, σ is the surface tension and U_i is the magnitude of velocity in cell i. This was extracted for each time step in the simulation, with the capillary number distribution shown in Fig. 4(c).

3. Results & Discussion

3.1. Validation of VoF using CT data

Water from the simulation and CT data for the Toray GDL was compared using a simulation domain shown in Fig. 2(b). This used the catalyst active area shown in yellow in Fig. 4(a) as the inlet area for water into the porous domain. The rest of the catalyst area was assumed as a wall in the simulation.

Fig. 4(a) shows the renderings of volume comparison between the CT water data and simulation data mapped onto the CT voxel grid different time steps. This also includes the water volume difference operation (where the translucent volume shows the matching water volume). This shows that the VoF simulation can predict water distribution at different time scales well if given the pore-scale microstructure. At water breakthrough to the gas channel, the results in Fig. 4(b) show there is between 58%–88% match in terms of spatial distribution of water. The accuracy is lower at earlier water production times because the water in the CT data invaded some pathways in a different order compared to the simulation data. Furthermore, the reason for lower water volume percentage match at the early times is also due to the fact that there are less water voxels in the domain and therefore differences in a few voxels contribute more to the overall volume percentage difference. The green volume shown in Fig. 4(b) is the filtered regions which the simulation did not have access to and was the consequence of the assumption of a liquid water inlet from the catalyst active area. This green volume, found by the voxels of water from CT images that the simulation never entered, are removed for the comparison in Fig. 4(a). Fig. 4(d) shows there is only a minor difference in the breakthrough location to the channel.

It is important to note that in each of these comparison cases, the saturation in the GDL was the same, but the distribution of water in the domain was different. Therefore, by comparing water volumes voxel to voxel, the model is being tested most rigorously. The most important data is at breakthrough to the channel (e.g. at 120 s in Fig. 4(a)) as this is when the water phase pressure is controlled by the droplet in the channel and relatively little movement of water in the GDL will occur. With that in mind, if VoF can replicate this distribution reasonably well, such as shown by the comparison between red and blue water clusters in Fig. 4(a), then this will be the most important criteria to test VoF accuracy against.

The comparison between the filtered and unfiltered comparison in Fig. 4(b) shows that the transient simulation does not match well with transient CT data (in terms of exact interface topology) without filtering. However, in this complex porous structure differences between simulation and experimental domains can deviate the water growth by the introduction or removal of important pore-scale features. In each comparison scenario, the volume of water in the GDL was almost matching it is only the distribution of that water volume that was different.

Compared to the VoF simulation of water injection in SGL 25 BA used in previous studies [23], the studied GDL structure (Toray TGP-H 060) and water clusters are more complex and the pores and throats are smaller but resolved at a similar voxel size. This fibrous system is therefore more prone to structure coarsening during the transcription process since some critical path defining features may only be 1 voxel in size.

The local scale capillary number distribution is shown in Fig. 4(c), where the capillary number is calculated using Eq. (10) for cells containing water at all time steps. The inlet area capillary number is shown by the black dashed line and the stability limit for capillary dominated water topology is shown by the red dashed line [44]. The distribution shows that the mean capillary number is around 4×10^{-3} and therefore there could be an influence of viscous forces which will change the fluid distribution pathways compared to a purely surface tension driven scenario. Although, in every pore scale system the pore scale velocity is much larger than the domain averaged velocity due to the reduced area of pore throats for flow (e.g. in the Hagen–Poiseuille equation, the mean velocity is half of the maximum velocity in the cross-section). Regardless, it was the assumption taken at the time which was able to replicate the general water distribution pattern at breakthrough to the channel.

The differences between VoF and CT water volume distribution could also be attributed to internal heterogeneous wettability [45], as is shown by the estimated real distribution of contact angles in the material in Fig. 5. Alternatively, the differences can be caused by the connected liquid water pathways in the CL [12]. This arises from the simulation either ignoring or simplifying these properties (e.g. isothermal conditions, homogeneous wettability, unresolved CL porous network). Nevertheless, the general water pore network remains the same between simulation and CT data as shown by Fig. 4(a). The simplifications used in this investigation were able to reproduce the water cluster accurate enough, resulting a small error but with greater computational efficiency. Consequently, this means that the VoF method can be used with confidence as a good prediction of the real dynamic water transport in fuel cell GDL. However, there are limits to the confidence of the model, highlighted by the need to identify the correct assumptions for water injection from the MPL, which could be from either percolation or phase change processes. Furthermore, the differences highlighted by the comparison in Fig. 4(b) and (d) show that the internal local scale wettability of the material, caused by the differences in coating methods and surface microstructure can alter the percolation pathways and this should be considered in future models.

The confidence of the CFD model is likely closer to the 88% accuracy because if the sources of water can be explicitly known (either by resolving the MPL void space, or as a condensation source), the other pathways not invaded by the simulation will be resolved. Furthermore, the assumptions made in the model for homogeneous pore-scale wettability can be improved by knowing explicitly the distribution of

contact angles inside the material. However, this information prior to experiments is hardly known and therefore a model that can estimate water percolation pathways like VoF can be useful for material design for the GDL, MPL and channels combined. Furthermore, the volume of water inside the GDL (saturation) in both the simulations and the experiment was the same, but it was the spatial distribution of that water that differed in Fig. 4(b).

3.2. Water injection and wettability analysis of Toray GDL

The results shown by the validation of the contact angle extraction code is shown in Fig. 5(a). This analysis at the full range of contact angles shows that the code can predict the mean contact angle reasonably well. However, there is greater variation in accuracy at low and high contact angles. Nevertheless, the contact angle under predicts hydrophobic contact angles and over predicts hydrophilic contact angles. This should result in a more normal distribution around neutral contact angle and could explain the shift in contract angle distributions found by the extraction on the CT data in Fig. 5(b). Regardless, the code was deemed sufficient due to its computational speed on each timestep (30 s per stack).

The code to extract the 3D contact angles was applied to each vertex where the water voxels interacted with the solid voxels, as shown by the spheres plotted on the surface in Fig. 5(c). It is clear from the image, that there is a spatial variation in the contact angles in the porous microstructure with some areas being correlated to being more hydrophobic or hydrophilic, shown by the difference in colours. These points are averaged values over 120 time steps and produce the distribution of contact angles as shown in Fig. 5(b). This shows that around 80% of the surface is hydrophobic, with a mean contact angle of 118° but also shows that around 20% of the surface is hydrophilic. These regions may cause wicking and retention into certain areas of the porous microstructure due to higher capillary adhesion forces as has been experimentally witnessed [19]. There is a difference in the distribution of contact angles found using the dynamic water CT data in this study to the data from Liu et al. 2021 [45]. However, both distributions show a higher fraction towards hydrophobic internal contact angles especially with increased PTFE coating including the observation that the mean contact angle (118°) is much lower than the apparent (sessile drop) contact angle by around 40°. The differences in our extraction in internal contact angles can be attributed to the predictive capability of the quick matlab contact angle calculator as shown by Fig. 5(a) including the unknown distribution of PTFE in both materials.

Considering the equilibrium contact angle of carbon and PTFE is around 66° [55] and 130° [56] respectively, then the local scale contact angles that exist beyond these ranges could be due to the resolution of the CT data not being high enough and so the code does not extract the angle correctly. Alternatively, these extreme contact angles could be extracted by a combination of the complex microstructure and wetting dynamics. For example the advancing contact angle of water on carbon can reach as high as 92° [55] and the receding as low as 40° [57]. With this in mind, the distribution of PTFE and internal wettability warrants further investigation, as local scale wettability differences can be manipulated to create materials with better water management properties [58].

To investigate the formation of water clusters in the Toray material, a full area water injection simulation (constant flux) was performed. Fig. 5(c) shows the water interface at different times, showing the emergence of several water clusters branches from the injection source. This is possible because the water phase pressure is large enough to enter some of the larger pores in the material.

In this case, many individual water clusters emerge prior to the onset of further in-plane movement. The in-plane movement leads to coalescence of clusters, forming fewer, larger clusters at later times close to breakthrough to the channel as shown in Fig. 5(d).

The in-plane movement and merging of water clusters is clear from the dynamic response of the water cluster density (the number of discrete clusters divided by the in-plane area). When the water clusters reach the channel (2×10^{-3} s), further in-plane merging is suppressed which is shown by the plateau of the saturation and water cluster density. This effect is caused by the decrease in the capillary pressure, caused by the open channel space [12]. This result highlights that using a thicker GDL could result in more in-plane merging, and therefore more stagnant water clusters.

3.3. Microporous layer crack inlet simulations

In this section, inlet boundary condition for water at the microporous layer is defined by controlling the cracking ratio (ratio of the crack area to MPL area) as shown in Fig. 2. These water injection simulations are performed to understand potential impact of MPL mechanical degradation on water flooding in the GDL. The simulations are continued until the saturation in the porous domain remains steady. The generated crack diameter size distribution is shown in Fig. 3(b). The crack propagation and size increases with MPL area coverage (2%–14%) with dimensions similar cracks found in literature [26,29] (average 60 μm crack width).

Fig. 6(a) shows the thickness of water for each simulation corresponding to crack dilations of 2, 8 and 14% respectively which is shown in Fig. 3(c). The 100% result (i.e. equivalent to no MPL) is taken from the final time of Fig. 5(e) and acts as the baseline case against which the varying crack dilation can be measured. The colour scale in Fig. 6 is significant because three-dimensional water volume data is mapped onto a two-dimensional grid. This allows the thickness (i.e. how much water is accumulated) to be shown rather than just water blockage, where white areas contain no water, and blue areas may only contain 1–2 voxels of water. The water volume difference between each crack area fractions simulations (increased crack dilation), shows that increasing the crack propagation (MPL area fraction) changes the distribution of water in the GDL.

When the same cracks are dilated (i.e. grown) by some physical process this enables the water network to have greater options for pores with lower entry capillary pressure. This can allow for entirely new clusters (shown by large water thickness (red)) or for connectivity between MPL cracks as shown by the water volume subtraction images in Fig. 6(a). The difference in cluster formation is particularly marked when comparing the 14% crack dilation case to that of the full water injection; there are water clusters in the 14% crack dilation case that do not appear in the 100% and vice versa. This suggests that the MPL cracks can alter the development of water clusters in GDL. Hence, ex-situ analysis (such as capillary pressure-saturation curves) may not fully represent how the material handles water during cell operation since it will overestimate GDL saturation.

Increasing the MPL crack area coverage increases the saturation of the GDL as shown by the saturation profiles in Fig. 6(b) and therefore in an optimal scenario, water injection sites to the GDL should be controlled. There is a sharp increase in saturation from the MPL apart from the 100% case which appears to result in a different saturation profile than the MPL crack cases. This difference is a result of the unrealistic conditions set up in the full water injection case; 100% injection is an extreme boundary condition unlikely in PEFC, since there would be no access for oxygen diffusion into the CL and thus represents a near limiting current case. These simulation results are based on the assumption of only water percolation from the MPL cracks whereas during PEFC operation, condensation of water vapour under the rib regions can be an additional source of water [14]. These results are important as they highlight the importance of the MPL in determining the water management characteristics of GDLs.

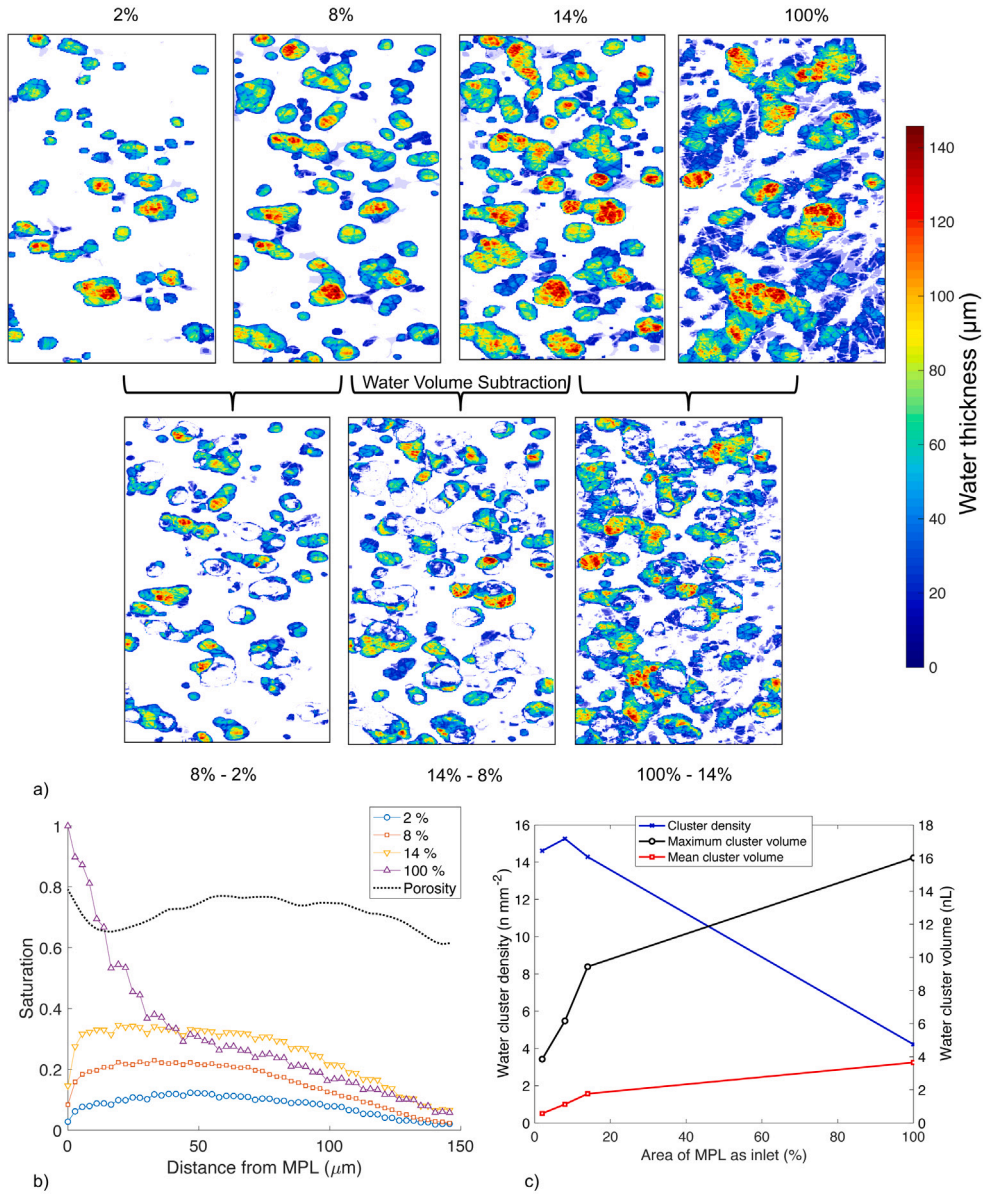

Fig. 6. Results of the water injection into a Toray material from MPL cracks for: (a) Through-plane water thickness (μm) for the final time step of each MPL crack scenario (2%–100%) with white showing no water present. Images below show the water volume subtraction process between each cracking ratio (e.g. 8% subtract 2%) revealing water distribution differences as cracking increases. (b) Saturation of the GDL as a function of the distance from the MPL. (c) Extracted water cluster density, mean and maximum cluster volumes for each simulation case. (For interpretation of the references to colour in this figure legend, the reader is referred to the web version of this article.)

3.4. Capillary pressure characteristics of discrete clusters

For the 2% crack area simulation, isolated cluster mechanisms have been extracted for a single water cluster under the rib as shown by Fig. 7(a) during its percolation and detachment cycle shown in Fig. 7(b). The capillary pressure of the water increases between points 1 to 2 where the critical pore throat produces the largest phase pressure in order to break through. Pore-scale invasion continues at lower capillary pressure between points 2 to 4 where the cluster merges with an adjacent cluster (shown by the jump in water volume).

The water attaches to the channel rib region between point 4 and 5 which reduces the phase pressure due to the decrease of interface curvature. This relaxation in pressure causes the connected water column to snap off as shown by the jump in capillary pressure at point 5 in Fig. 7. Point 6 represents the similar scenario as point 1. This mechanism of water removal is an important feature of hydrophilic channels, therefore a design of a PEFC with hydrophobic channel features will not benefit from this water removal technique. The phase pressure profile obtained for this cluster is similar in phase pressure magnitude (between 3–6 kPa) to the results found by [12].

However, the simulation most likely overestimates the evacuation of water out of the structure due to the use of a single contact angle for the GDL. This does not account for the receding contact angle which will resist water movement out of the GDL, this has been shown in the differences between simulation and experimental results [23,59].

3.5. Oxygen distribution at MPL surface

To show the impact of water flooding and microstructure on PEFC performance, two simulations were performed under single-phase and two-phase conditions (using the last time of the 14% MPL crack case). In the two-phase case, the water surface was considered to be a solid surface. The velocity field from solving the steady state momentum equation was used to solve the advective–diffusive transport equation with a fixed gradient boundary condition at the MPL surface. This

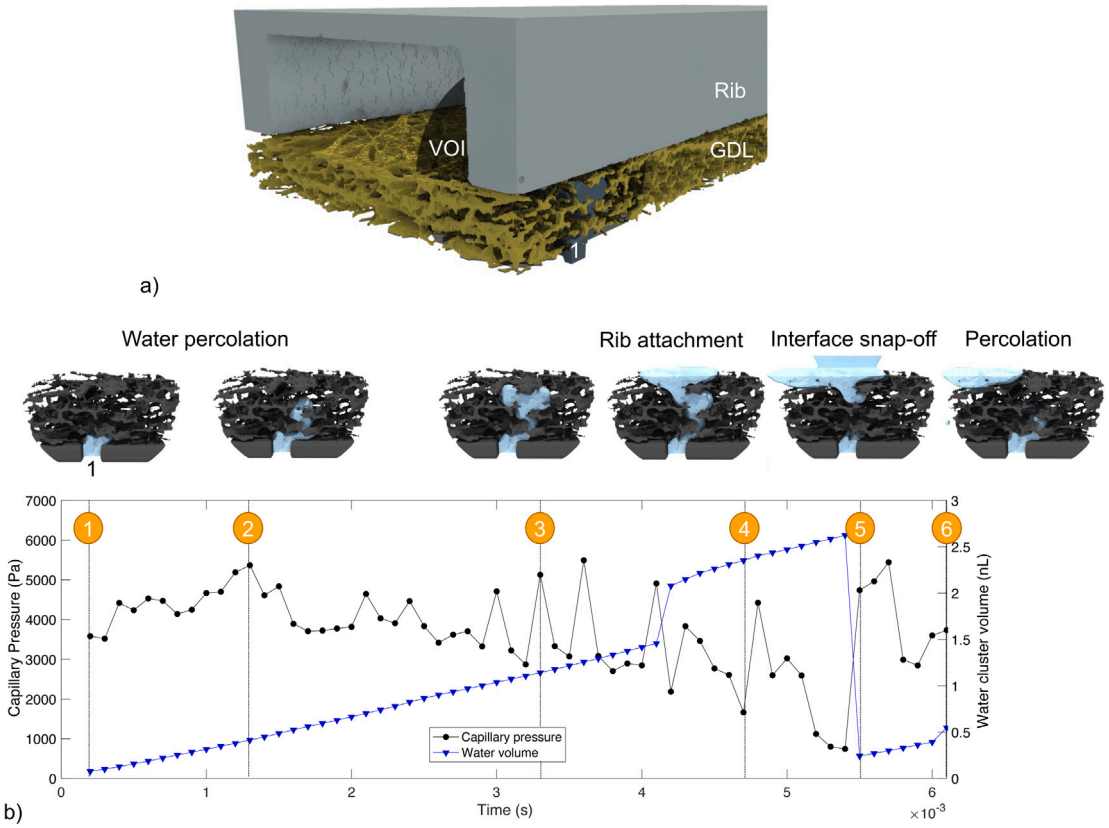

Fig. 7. (a) 3D rendering of X-ray data removing the void space showing the rib, GDL and spherical volume of interest (VOI) for the following analysis. (b) Capillary pressure ($P_c = P_{water} - P_{air}$) and water cluster volume profiles over time for water percolation with P_c variation from pore invasion (1–3), channel rib attachment (4) and interface snap off (5) processes.

approximates the consumption of oxygen as a diffusive flux through the boundary based on the current density (1 A cm^{-2}) [5].

The velocity, pressure and oxygen concentration field through the two-phase domain is shown in Fig. 8(a). The distribution of the velocity due to the acceleration around droplets and low flux in the GDL creates dispersion in the oxygen distribution, as shown by the differences in concentration at the channel surface and at the MPL surface as shown in Fig. 8(b). The presence of water clusters can create transport resistance to areas directly beneath but also adjacent to each cluster.

The impact of both microstructure and water on the oxygen transport can be seen in the oxygen distribution at the MPL surface for single-phase and two-phase flow shown in Fig. 8(c). As discussed earlier, in Fig. 6, the in-plane merging of water clusters can create resistance for oxygen transport. This effect can be clearly seen in regions between some of the MPL cracks which show reduction in oxygen concentration by 10 to 15% compared to the single phase case. The variation in oxygen concentration in PEFC operation will cause large temperature profile variance, leading to more local degradation. Although this is not studied in this work, future modelling work could investigate the effect of these local gradients on the performance. Fig. 8(d) shows the averaged oxygen concentration along the length of the channel; the presence of water decreases the average concentration at the MPL surface by about 3% compared to the single phase case, due to the added transport resistance from the water. Although this value is small, we only considered a small domain size (mm) in comparison to the full cell area and at higher current density with less convection in the channel, this variation in oxygen concentration could be higher.

This phenomena is important to consider for the design of new GDL and MPL materials. For an optimal water removal, water should feature low in-plane movement to restrict the impact of water on oxygen transport to the MPL surface. Introduction of more convection into the GDL could reduce the large gradients in oxygen, which could be achieved by more open pore structures [5,60].

4. Conclusion

In this study CFD simulations have been used in a segmented X-ray CT image of a Toray material to understand the impact of injection conditions formed by the microporous layer (MPL) on the water clusters formed in the GDL. The artificial cracking of the MPL was used to understand the potential consequences of material degradation. The use of VoF was analysed against exact water volume data in an operando experiment, showing a 58%–88% match at water breakthrough to the channel. This result improves the confidence in the use of CFD for predicting water distribution in pore-scale materials in PEFC.

Using a quick image analysis code, the 3D averaged contact angle was found for the internal surfaces which showed that around 80% of the surface was hydrophobic with a mean contact angle of 118°. The water cluster density was shown to be between 5–15 n mm^{-2} and depends on the water source condition from the MPL interface. This value has been shown to be an important condition for two-phase flow simulations in the flow channels [1].

An MPL with increasing crack dilation will increase GDL water flooding due to greater options and probability for the connected water network to flow (resulting in more in-plane movement before breakthrough to the channel). The presence of an MPL was shown to create main water cluster pathways (14% crack area) that were not replicated by the GDL without an MPL (100% crack area). Consequently, the results presented in this study highlight the importance of minimising microporous layer cracking; since the 2% area boundary condition resulted in a lower overall saturation. Furthermore, the results highlight that using a thinner GDL may limit the in-plane coalescence of clusters.

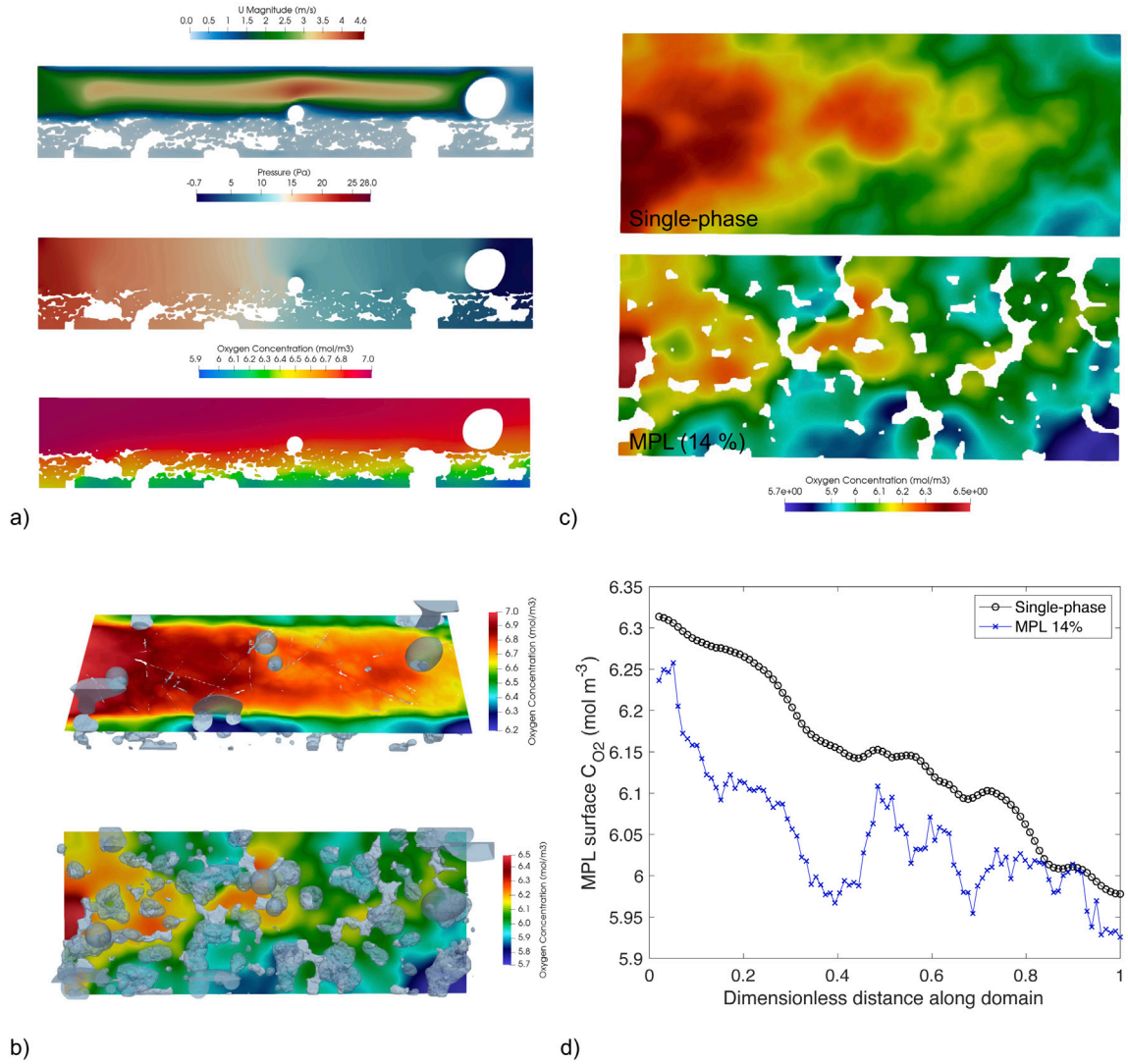

Fig. 8. (a) steady state velocity field, pressure field and oxygen concentration for a slice through the simulation domain with 14% MPL cracking. (b) Rendering of water volume effect on the oxygen distribution in the channel and at the MPL surface. (c) Differences between oxygen distribution at the MPL between single-phase and two-phase flow. (d) Averaged concentration of oxygen along the length of the channel at the MPL surface for single-phase and two-phase flow (14% cracked).

This study also showed that the boundary conditions for water injection into the GDL can create different water distributions.

The effect of the water clusters on oxygen distribution was simulated using a scalar consumption boundary condition at the CL surface which showed that locally there could be a minimum of 10% difference compared to the single-phase case. This is caused by the in-plane extent of some water clusters between MPL cracks and therefore, it is important to limit water cluster growth in the in-plane direction. This could be made possible through the use of porous microstructure design [5] and or patterned wettability alteration [58].

Future work should consider firstly if the distribution of MPL cracks can be controlled and secondly to select a cracking arrangement that minimises water cluster merging, subsequently reducing the impact of in-plane water spreading on the oxygen transport to the CL. Further simulation studies could investigate the effect of local oxygen concentration on the temperature variation and subsequent degradation of the cell.

CRediT authorship contribution statement

Daniel Niblett: Conceptualization, Methodology, Software, Validation, Formal analysis, Investigation, Writing – original draft, Writing – review & editing, Visualization, Funding acquisition. **Vahid Niasar:** Conceptualization, Supervision, Writing – original draft, Funding acquisition. **Stuart Holmes:** Supervision, Writing – original draft. **Adrian Mularczyk:** Conceptualization, Validation, Resources, Data curation, Writing – original draft. **Jens Eller:** Conceptualization, Validation, Resources, Data curation, Writing – original draft. **Robert Prosser:** Supervision, Methodology, Writing – original draft, Funding acquisition. **Mohamed Mamlouk:** Supervision, Writing – review & editing, Resources, Funding acquisition.

Declaration of competing interest

The authors declare that they have no known competing financial interests or personal relationships that could have appeared to influence the work reported in this paper.

Data availability

Data will be made available on request.

Acknowledgements

The authors would like to acknowledge the UK Engineering and Physical Sciences Research Council (EPSRC) for funding the PhD study and EPSRC Doctoral Prize Fellowship of Daniel Niblett (NPIF EPSRC EP/R512394/1) and the Swiss National Science Foundation (SNF project no. 153790) for funding the PhD study of Adrian Mularczyk.

References

[1] D. Niblett, S.M. Holmes, V. Niasar, Discrete-particle model to optimize operational conditions of proton-exchange membrane fuel-cell gas channels, ACS Appl. Energy Mater. 4 (2021) 10514–10533.

[2] A.Z. Weber, R.L. Borup, R.M. Darling, P.K. Das, T.J. Dursch, W. Gu, D. Harvey, A. Kusoglu, S. Litster, M.M. Mench, R. Mukundan, J.P. Owejan, J.G. Pharoah, M. Secanell, I.V. Zenyuk, A critical review of modeling transport phenomena in polymer-electrolyte fuel cells, J. Electrochem. Soc. 161 (12) (2014) F1254–F1299.

[3] J.T. Gostick, M.A. Ioannidis, M.W. Fowler, M.D. Pritzker, Pore network modeling of fibrous gas diffusion layers for polymer electrolyte membrane fuel cells, J. Power Sources 173 (1) (2007) 277–290.

[4] B. Tjaden, D.J.L. Brett, P.R. Shearing, Tortuosity in electrochemical devices: a review of calculation approaches, Int. Mater. Rev. 63 (2) (2018) 47–67, [Online]. Available: https://doi.org/10.1080/09506608.2016.1249995.

[5] D. Niblett, Z. Guo, S. Holmes, V. Niasar, R. Prosser, Utilization of 3D printed carbon gas diffusion layers in polymer electrolyte membrane fuel cells, Int. J. Hydrogen Energy (2022) [Online]. Available: https://www.sciencedirect.com/science/article/pii/S0360319922021978.

[6] R.B. Ferreira, D.S. Falcão, V.B. Oliveira, A.M. Pinto, 1D + 3D two-phase flow numerical model of a proton exchange membrane fuel cell, Appl. Energy 203 (2017) 474–495.

[7] S. Culubret, M.A. Rubio, D.G. Sanchez, A. Urquia, Dynamic modeling of the effect of water management on polymer electrolyte fuel cells performance, Int. J. Hydrogen Energy 45 (9) (2020) 5710–5722, [Online]. Available: https://doi.org/10.1016/j.ijhydene.2019.07.176.

[8] J. Yu, D. Froning, U. Reimer, W. Lehnert, Liquid water breakthrough location distances on a gas diffusion layer of polymer electrolyte membrane fuel cells, J. Power Sources 389 (October 2017) (2018) 56–60, [Online]. Available: https://doi.org/10.1016/j.jpowsour.2018.04.004.

[9] H. Markötter, I. Manke, J.H. mann, T. Arlt, M. Klages, P. Krüger, C. Hartnig, J. Scholta, B. Müller, H. Riesemeier, J. Banhart, Combined synchrotron X-ray radiography and tomography study of water transport in gas diffusion layers, Micro Nano Lett. 7 (2012) [Online]. Available: https://digital-library.theiet.org/content/journals/10.1049/mnl.2012.0410, 689–692(3).

[10] K. Tüber, D. Pócza, C. Hebling, Visualization of water buildup in the cathode of a transparent PEM fuel cell, J. Power Sources 124 (2) (2003) 403–414, [Online]. Available: https://www.sciencedirect.com/science/article/pii/S0378775303007973.

[11] M. Bodner, A. Schenk, D. Salaberger, M. Rami, C. Hochenauer, V. Hacker, Air starvation induced degradation in polymer electrolyte fuel cells, Fuel Cells 17 (1) (2017) 18–26, [Online]. Available: https://onlinelibrary.wiley.com/doi/abs/10.1002/fuce.201600132.

[12] A. Mularczyk, Q. Lin, D. Niblett, A. Vasile, M.J. Blunt, V. Niasar, F. Marone, T.J. Schmidt, F.N. Büchi, J. Eller, Operando liquid pressure determination in polymer electrolyte fuel cells, ACS Appl. Mater. Interfaces (2021) null, [Online]. Available: https://doi.org/10.1021/acsami.1c04560, PMID: 34235914.

[13] J. Hack, L. Rasha, P.L. Cullen, J.J. Bailey, T.P. Neville, P.R. Shearing, N.P. Brandon, D.J. Brett, Use of X-ray computed tomography for understanding localised, along-the-channel degradation of polymer electrolyte fuel cells, Electrochim. Acta 352 (2020) 136464, [Online]. Available: https://doi.org/10.1016/j.electacta.2020.136464.

[14] H. Xu, S. Nagashima, H.P. Nguyen, K. Kishita, F. Marone, F.N. Büchi, J. Eller, Temperature dependent water transport mechanism in gas diffusion layers revealed by subsecond operando X-ray tomographic microscopy, J. Power Sources 490 (December 2020) (2021) 229492, [Online]. Available: https://doi.org/10.1016/j.jpowsour.2021.229492.

[15] Z. Niu, Y. Wang, K. Jiao, J. Wu, Two-phase flow dynamics in the gas diffusion layer of proton exchange membrane fuel cells: Volume of fluid modeling and comparison with experiment, J. Electrochem. Soc. 165 (9) (2018) F613–F620.

[16] B. Straubhaar, J. Pauchet, M. Prat, Pore network modelling of condensation in gas diffusion layers of proton exchange membrane fuel cells, Int. J. Heat Mass Transfer 102 (2016) 891–901.

[17] M. Aghighi, J. Gostick, Pore network modeling of phase change in PEM fuel cell fibrous cathode, J. Appl. Electrochem. 47 (12) (2017) 1323–1338.

[18] J. Eller, J. Roth, F. Marone, M. Stampanoni, F.N. Büchi, Operando properties of gas diffusion layers: Saturation and liquid permeability, J. Electrochem. Soc. 164 (2) (2017) F115–F126.

[19] P. Shrestha, C. Lee, K.F. Fahy, M. Balakrishnan, N. Ge, A. Bazylak, Formation of liquid water pathways in PEM fuel cells: A 3-D pore-scale perspective, J. Electrochem. Soc. 167 (5) (2020) 054516.

[20] P. Krüger, H. Markötter, J.H. mann, M. Klages, T. Arlt, J. Banhart, C. Hartnig, I. Manke, J. Scholta, Synchrotron X-ray tomography for investigations of water distribution in polymer electrolyte membrane fuel cells, J. Power Sources 196 (2011) 5250–5255.

[21] S.J. Normile, D.C. Sabarirajan, O. Calzada, V.D. Andrade, X. Xiao, P. Mandal, D.Y. Parkinson, A. Serov, P. Atanassov, I.V. Zenyuk, Direct observations of liquid water formation at nano- and micro-scale in platinum group metal-free electrodes by operando X-ray computed tomography, Mater. Today Energy 9 (2018) 187–197.

[22] A. Mularczyk, Q. Lin, M.J. Blunt, A. Lamibrac, F. Marone, T.J. Schmidt, F.N. Büchi, J. Eller, Droplet and percolation network interactions in a fuel cell gas diffusion layer, J. Electrochem. Soc. 167 (8) (2020) 084506, [Online]. Available: https://doi.org/10.1149/1945-7111/ab8c85.

[23] D. Niblett, A. Mularczyk, V. Niasar, J. Eller, S. Holmes, Two-phase flow dynamics in a gas diffusion layer - gas channel - microporous layer system, J. Power Sources 471 (2020) 228427, [Online]. Available: https://doi.org/10.1016/j.jpowsour.2020.228427.

[24] P. Satjaritanun, S. Shimpalee, I.V. Zenyuk, Gas diffusion layers: Experimental and modeling approach for morphological and transport properties, Acc. Mater. Res. 3 (4) (2022) 416–425, [Online]. Available: https://doi.org/10.1021/accountsmr.1c00125.

[25] D. Niblett, V. Joekar-Niasar, S. Holmes, Enhancing the performance of fuel cell gas diffusion layers using ordered microstructural design, J. Electrochem. Soc. 167 (7) (2018) 013520.

[26] R.T. White, S.H. Eberhardt, Y. Singh, T. Haddow, M. Dutta, F.P. Orfino, E. Kjeang, Four-dimensional joint visualization of electrode degradation and liquid water distribution inside operating polymer electrolyte fuel cells, Sci. Rep. 9 (1) (2019) 1–13.

[27] R.T. White, D. Ramani, S. Eberhardt, M. Najm, F.P. Orfino, M. Dutta, E. Kjeang, Correlative X-ray tomographic imaging of catalyst layer degradation in fuel cells, J. Electrochem. Soc. 166 (13) (2019) F914–F925.

[28] F.C. Cetinbas, R.K. Ahluwalia, A.D. Shum, I.V. Zenyuk, Direct simulations of pore-scale water transport through diffusion media, J. Electrochem. Soc. 166 (7) (2019) F3001–F3008.

[29] F.E. Hizir, S.O. Ural, E.C. Kumbur, M.M. Mench, Characterization of interfacial morphology in polymer electrolyte fuel cells: Micro-porous layer and catalyst layer surfaces, J. Power Sources 195 (11) (2010) 3463–3471.

[30] J. Halter, F. Marone, T.J. Schmidt, F.N. Büchi, Breaking through the cracks: On the mechanism of phosphoric acid migration in high temperature polymer electrolyte fuel cells, J. Electrochem. Soc. 165 (14) (2018) F1176–F1183.

[31] N. Bevilacqua, M.G. George, S. Galbiati, A. Bazylak, R. Zeis, Phosphoric acid invasion in high temperature PEM fuel cell gas diffusion layers, Electrochim. Acta 257 (2017) 89–98.

[32] P. Satjaritanun, J.W. Weidner, S. Hirano, Z. Lu, Y. Khunatorn, S. Ogawa, S.E. Litster, A.D. Shum, I.V. Zenyuk, S. Shimpalee, Micro-scale analysis of liquid water breakthrough inside gas diffusion layer for PEMFC using X-ray computed tomography and lattice Boltzmann method, J. Electrochem. Soc. 164 (11) (2017) E3359–E3371.

[33] J. Cho, S. Lee, B.S. Shim, J.S. Yi, D. Kim, S. Park, Unveiling water drainage through microporous layer with laser-ablated open furrows in proton exchange membrane fuel cells, J. Power Sources 491 (January) (2021) 229563, [Online]. Available: https://doi.org/10.1016/j.jpowsour.2021.229563.

[34] M. Fazeli, J. Hinebaugh, Z. Fishman, C. Tötzke, W. Lehnert, I. Manke, A. Bazylak, Pore network modeling to explore the effects of compression on multiphase transport in polymer electrolyte membrane fuel cell gas diffusion layers, J. Power Sources 335 (2016) 162–171.

[35] J. Hinebaugh, J. Lee, C. Mascarenhas, A. Bazylak, Quantifying percolation events in PEM fuel cell using synchrotron radiography, Electrochim. Acta 184 (2015) 417–426, [Online]. Available: https://www.sciencedirect.com/science/article/pii/S0013468615304709.

[36] M. Andersson, A. Mularczyk, A. Lamibrac, S.B. Beale, J. Eller, W. Lehnert, F.N. Büchi, Modeling and synchrotron imaging of droplet detachment in gas channels of polymer electrolyte fuel cells, J. Power Sources 404 (October) (2018) 159–171, [Online]. Available: https://doi.org/10.1016/j.jpowsour.2018.10.021.

[37] M. Andersson, S.B. Beale, U. Reimer, W. Lehnert, D. Stolten, Interface resolving two-phase flow simulations in gas channels relevant for polymer electrolyte fuel cells using the volume of fluid approach, Int. J. Hydrogen Energy 43 (5) (2018) 2961–2976, [Online]. Available: https://doi.org/10.1016/j.ijhydene.2017.12.129.

[38] L. Gamet, M. Scala, J. Roenby, H. Scheufler, J.-L. Pierson, Validation of volume-of-fluid OpenFOAM® isoadvector solvers using single bubble benchmarks, Comput. & Fluids 213 (2020) 104722, [Online]. Available: https://www.sciencedirect.com/science/article/pii/S0045793020302929.

[39] T.G. Tranter, P. Boillat, A. Mularczyk, V. Manzi-Orezzoli, P.R. Shearing, D.J.L. Brett, J. Eller, J.T. Gostick, A. Forner-Cuenca, Pore network modelling of capillary transport and relative diffusivity in gas diffusion layers with patterned wettability, J. Electrochem. Soc. 167 (11) (2020) 114512.

[40] T. Agaesse, A. Lamibrac, F.N. Büchi, J. Pauchet, M. Prat, Validation of pore network simulations of ex-situ water distributions in a gas diffusion layer of proton exchange membrane fuel cells with X-ray tomographic images, J. Power Sources 331 (2016) 462–474.

[41] N. Zhan, W. Wu, S. Wang, Pore network modeling of liquid water and oxygen transport through the porosity-graded bilayer gas diffusion layer of polymer electrolyte membrane fuel cells, Electrochim. Acta 306 (2019) 264–276, [Online]. Available: https://doi.org/10.1016/j.electacta.2019.03.115.

[42] N. Belgacem, M. Prat, J. Pauchet, Coupled continuum and condensation–evaporation pore network model of the cathode in polymer-electrolyte fuel cell, Int. J. Hydrogen Energy 42 (12) (2017) 8150–8165.

[43] I.V. Zenyuk, E. Medici, J. Allen, A.Z. Weber, Coupling continuum and pore-network models for polymer-electrolyte fuel cells, Int. J. Hydrogen Energy 40 (46) (2015) 16831–16845.

[44] S. Sakaida, Y. Tabe, T. Chikahisa, Large scale simulation of liquid water transport in a gas diffusion layer of polymer electrolyte membrane fuel cells using the lattice Boltzmann method, J. Power Sources 361 (2017) 133–143, [Online]. Available: http://dx.doi.org/10.1016/j.jpowsour.2017.06.054.

[45] C.P. Liu, P. Saha, Y. Huang, S. Shimpalee, P. Satjaritanun, I.V. Zenyuk, Measurement of contact angles at carbon fiber–water–air triple-phase boundaries inside gas diffusion layers using X-ray computed tomography, ACS Appl. Mater. Interfaces 13 (17) (2021) 20002–20013.

[46] A. Bazylak, D. Sinton, N. Djilali, Dynamic water transport and droplet emergence in PEMFC gas diffusion layers, J. Power Sources 176 (1) (2008) 240–246.

[47] S. An, H. Erfani, O.E. Godinez-Brizuela, V. Niasar, Transition from viscous fingering to capillary fingering: Application of GPU-based fully implicit dynamic pore network modeling, Water Resour. Res. 56 (12) (2020) e2020WR028149, [Online]. Available: https://agupubs.onlinelibrary.wiley.com/doi/abs/10.1029/2020WR028149, e2020WR028149 10.1029/2020WR028149.

[48] S. An, H. Yu, J. Yao, GPU-accelerated volumetric lattice Boltzmann method for porous media flow, J. Pet. Sci. Eng. 156 (2017) 546–552, [Online]. Available: https://www.sciencedirect.com/science/article/pii/S0920410517305260.

[49] S.S. Deshpande, L. Anumolu, M.F. Trujillo, Evaluating the performance of the two-phase flow solver interfoam, Comput. Sci. Discov. 5 (1) (2012) http://dx.doi.org/10.1088/1749-4699/5/1/014016.

[50] M. Sabharwal, J.T. Gostick, M. Secanell, Virtual liquid water intrusion in fuel cell gas diffusion media, J. Electrochem. Soc. 165 (7) (2018) F553–F563, [Online]. Available: https://doi.org/10.1149/2.0921807jes.

[51] D. Niblett, M. Mamlouk, O.E.G. Brizuela, Porous microstructure generator, 2022, [Online]. Available: https://data.ncl.ac.uk/articles/software/Porous_Microstructure_Generator/20448471.

[52] J. Roenby, H. Bredmose, H. Jasak, A computational method for sharp interface advection, R. Soc. Open Sci. 3 (11) (2016).

[53] H. Jasak, A. Jemcov, Openfoam paper, in: International Workshop on Coupled Methods in Numerical Dynamics, Vol. m, 2007, pp. 1–20.

[54] S. Yu, X. Li, S. Liu, J. Hao, Z. Shao, B. Yi, Study on hydrophobicity loss of the gas diffusion layer in PEMFCs by electrochemical oxidation, RSC Adv. 4 (2014) 3852–3856, http://dx.doi.org/10.1039/C3RA45770B, [Online]. Available: http://dx.doi.org/10.1039/C3RA45770B.

[55] S. Qiu, C.A. Fuentes, D. Zhang, A.W. Van Vuure, D. Seveno, Wettability of a single carbon fiber, Langmuir 32 (38) (2016) 9697–9705, [Online]. Available: https://doi.org/10.1021/acs.langmuir.6b02072, PMID: 27547993.

[56] J. Włoch, A.P. Terzyk, M. Wiśniewski, P. Kowalczyk, Nanoscale water contact angle on polytetrafluoroethylene surfaces characterized by molecular dynamics–atomic force microscopy imaging, Langmuir 34 (15) (2018) 4526–4534, [Online]. Available: https://doi.org/10.1021/acs.langmuir.8b00257, PMID: 29528239.

[57] C. Lu, J. Wang, X. Lu, T. Zheng, Y. Liu, X. Wang, D. Zhang, D. Seveno, Wettability and interfacial properties of carbon fiber and poly(ether ether ketone) fiber hybrid composite, ACS Appl. Mater. Interfaces 11 (34) (2019) 31520–31531, [Online]. Available: https://doi.org/10.1021/acsami.9b09735, PMID: 31369238.

[58] A. Forner-Cuenca, J. Biesdorf, L. Gubler, P.M. Kristiansen, T.J. Schmidt, P. Boillat, Engineered water highways in fuel cells: Radiation grafting of gas diffusion layers, Adv. Mater. 27 (2015) 6317–6322.

[59] A. Mularczyk, Q. Lin, M.J. Blunt, A. Lamibrac, F. Marone, T.J. Schmidt, F.N. Büchi, J. Eller, Droplet and percolation network interactions in a fuel cell gas diffusion layer, J. Electrochem. Soc. 167 (8) (2020) 084506.

[60] J.E. Park, J. Lim, M.S. Lim, S. Kim, O.-H. Kim, D.W. Lee, J.H. Lee, Y.-H. Cho, Y.-E. Sung, Gas diffusion layer/flow-field unified membrane-electrode assembly in fuel cell using graphene foam, Electrochim. Acta 323 (2019) 134808, [Online]. Available: https://www.sciencedirect.com/science/article/pii/S0013468619316792.